Submitted to Cement and Concrete Research

Calcium aluminate cement conversion analysed by ptychographic nanotomography

S. Shirani[1],[#] A. Cuesta[1],[#] A. G. De la Torre[1], A. Diaz[2], P. Trtik[2], M. Holler[2], M. A. G. Aranda[1]*

[1]*Departamento de Química Inorgánica, Cristalografía y Mineralogía, Universidad de Málaga, Málaga, 29071, Spain.*

[2]*Paul Scherrer Institut, 5232 Villigen PSI, Switzerland*

[#] *These authors have contributed equally*

* *email: g_aranda@uma.es*

Abstract.

Calcium aluminate cements are used for special applications but are nowadays banned for general structural purposes due to the calcium aluminate hydrate conversion, that has led, for concretes fabricated with high water contents, to building collapses. The stoichiometries of these conversion chemical reactions are relatively well established but the consequences in porosity, key to predict durability, were unknown. Here, we have used hard X-ray ptychographic nanotomography to study the hydration of $CaAl_2O_4$ at different temperatures and chiefly, at 4ºC and then at 50ºC to provoke conversion similar to field conditions. The mass densities of the resulting $Al(OH)_3$ gels were 1.94, 1.98 and 2.23 $g{\cdot}cm^{-3}$, for samples hydrated at 4, 20 and 50ºC, respectively. These values are lower than that of gibbsite, 2.42 $g{\cdot}cm^{-3}$. Above all, this 3D imaging technique has allowed measuring the secondary water porosity developed in the conversion, which has an average pore dimension close to 140 nm.

Keywords: CAC conversion; volume stability; density measurement; X-ray synchrotron imaging; mesoscale;

1. Introduction.

Calcium aluminate cements (CACs) are used for several special applications. These cements have some distinctive properties such as high early strength development (even at low temperatures), high chemical resistance, very good performances when calcined at high temperatures and good workability at low temperatures [1]. CACs can produce high-performance concretes [2] and they are mainly used in refractory concretes [3], and also for acid attack resistance in industrial floors and sewage applications [4], as rapid repair materials [5] and as additions in complex formulations in the building industry. CACs are not recommended, and in many countries banned, for general structural purposes, as they are much more sensitive to misuse than Portland cements. Concretes made from CACs can show good long-term strength and durability for water-to-cement (w/c) mass ratios below 0.40 and cement content above 400 kg/m^3 [1]. However, lower cement contents and especially higher w/c ratios lead to severe durability problems with many building collapses documented all around the world. These problems are due to the CACs hydrate conversion as discussed next.

CACs are mainly produced out of limestone and bauxite with variable elemental and mineralogical compositions [1,2,6], but $CaAl_2O_4$ (monocalcium aluminate) is always the main hydraulic phase with contents higher than 40 wt%. Therefore, the full understanding of the hydration behaviour of monocalcium aluminate is of the utmost importance. It is well established that the hydration reactions of $CaAl_2O_4$ strongly depend on temperature [2], see Table 1. $CaAl_2O_4$ is abbreviated as CA ($CaO{\cdot}Al_2O_3$) following the standard cement notation, see Table 2, which is adopted hereafter. These chemical reactions are further detailed below including the densities of the resulting solids. The understanding of the mass density changes along these reactions is key to explain the conversion features that are observed in CACs mortars and concretes. It is known that the conversion reaction(s) invariably takes place with time, enhanced with any temperature increase. However, the durability of CACs binders is severely compromised when the w/c ratios of the concretes are higher than approximately 0.40.

Next, we develop the chemical reactions sketched in Table 1, see reactions (1) to (6), stating the molar masses and the volumes changes to the best of the current knowledge. The mass density values are required to determine the molar volumes. The mass densities used for CA, CAH_{10}, and C_3AH_6 are 2.96 [7], 1.72 [8,9] and 2.53 g·cm^{-3} [10], respectively. The density values of C_2AH_8 and $Al(OH)_3$ merit discussion. The full crystal structure of C_2AH_8 is still not known although this phase was firstly reported in 1900 [11] and its powder pattern is known since 1933 [12]. An initial value of 1.95 g·cm^{-3} was reported [13] which was gathered in standard texts [8,10] and very recently erroneously quoted as 1.75 g·cm^{-3} in [14]. Subsequently, the crystallographic density was reported as 1.91 g·cm^{-3} [15] based on the unit cell volume and chemical content. In [15], a crystallographic density of 1.96 g·cm^{-3} was reported for $C_2AH_{7.5}$ which is a slightly dehydrated form.

Aluminium hydroxide, $Al(OH)_3$ with gibbsite crystal structure, has a density of 2.42 g·cm^{-3} [10]. However, aluminium hydroxides precipitated in these hydration reactions have a variable crystallinity that evolves from amorphous to nanocrystalline to close to crystalline gibbsite (with increasing hydration temperatures). The mass densities of the aluminium hydroxide gels at the microscale are variable due to the lack of packing of the $Al(OH)_3$ set of layers [16] at the nanoscale. Furthermore, the micrometre size $Al(OH)_3$ gel particles could enclose gel pore water. The (gel) water content of nanocrystalline aluminium hydroxides will likely vary with hydrating temperature and possibly with the initial w/c ratio, and it is still unknown.

The chemical reactions (1) to (3) shown below correspond to the direct hydration of CA at increasing temperatures, see Table 1. Meanwhile, reaction (4) describes the conversion of metastable CAH_{10} to metastable C_2AH_8 and reaction (5) the conversion of C_2AH_8 to C_3AH_6, the stable phase in this system. Reaction (6) describes the densification/crystallization of $Al(OH)_3$ with time and/or temperature. It is emphasized that the densities for the crystalline phases are gathered

from the crystal structures and the densities for the $Al(OH)_3$ gels are those obtained in this work, see Table 2 below. These last three reactions [17] are generally quoted as *'conversion of CAC metastable hydrates'* and it has been very recently proved [18] that chemical reactions (4) and (5) proceed through a solution and precipitation mechanism and they do not take place in the absence of free water, therefore ruling out the possible mechanism based on solid-state reactions.

Table 1. Relevant chemical reactions in the hydration of calcium monoaluminate.

$CaAl_2O_4$	**+**	**10 H_2O**	**→**	**$CaAl_2O_4{\cdot}10H_2O$**				Mainly at T<15ºC	**(1)**
158.04		180.20		338.19				(g/mol)	
53.39 [ρ=*2.96 g·cm^{-3}*]		180.20		196.62 [ρ=*1.72 g·cm^{-3}*]				(cm^3/mol)	
Reactants: 233.59 cm^3. Products: 196.62 cm^3. Theoretical chemical shrinkage: -36.97 cm^3/mol or 15.8 %.									
2 $CaAl_2O_4$	**+**	**11 H_2O**	**→**	**$Ca_2Al_2O_5{\cdot}8H_2O$**	**+**	**2 $Al(OH)_3$ –gel–**		Mainly at T∈15-50ºC	**(2)**
316.08		198.22		358.24		156.00		(g/mol)	
106.78		198.22		187.56 [ρ=*1.91 g·cm^{-3}*]		78.00 [ρ~*2.00 g·cm^{-3}*]		(cm^3/mol)	
Reactants: 305.00 cm^3. Products: 265.56 cm^3. Theoretical chemical shrinkage: -39.44 cm^3/mol or 12.9 %.									
3 $CaAl_2O_4$	**+**	**12 H_2O**	**→**	**$Ca_3Al_2(OH)_{12}$**	**+**	**4 $Al(OH)_3$ –gel–**		Mainly at T>50ºC	**(3)**
474.12		216.24		378.29		312.00		(g/mol)	
160.18		216.24		149.52 [ρ=*2.53 g·cm^{-3}*]		141.82 [ρ~*2.20 g·cm^{-3}*]		(cm^3/mol)	
Reactants: 376.42 cm^3. Products: 291.34 cm^3. Theoretical chemical shrinkage: -85.08 cm^3/mol or 22.6 %.									
2 $CaAl_2O_4{\cdot}10H_2O$		**→**	**$Ca_2Al_2O_5{\cdot}8H_2O$**	**+**	**2 $Al(OH)_3$ –gel–**	**+**	**9 H_2O**	Mainly at T>15ºC	**(4)**
676.38			358.24		156.00		162.18	(g/mol)	
393.24			187.56		78.00 [ρ~*2.00 g·cm^{-3}*]		162.18	(cm^3/mol)	
Solid reactants: 393.24 cm^3. Solid products: 265.56 cm^3. Secondary water porosity: 162.18 cm^3 or 37.9%									
3 $Ca_2Al_2O_5{\cdot}8H_2O$		**→**	**2 $Ca_3Al_2(OH)_{12}$**	**+**	**2 $Al(OH)_3$ –gel–**	**+**	**9 H_2O**	Mainly at T>50ºC	**(5)**
1074.72			756.58		156.00		162.18	(g/mol)	
562.68			299.04		70.91 [ρ~*2.20 g·cm^{-3}*]		162.18	(cm^3/mol)	
Solid reactants: 562.68 cm^3. Solid products: 369.95 cm^3. Secondary water porosity: 162.18 cm^3 or 28.8%									
$Al(OH)_3$ –gel (n H_2O?)–		**→**	**$Al(OH)_3$ –gibbsite–**	**+**	**n H_2O**			T-dependent	**(6)**
78.00+??			78.00		??			(g/mol)	
39.00+?? [ρ~*2.00 g·cm^{-3}*]			32.23 [ρ=*2.42 g·cm^{-3}*]		??			(cm^3/mol)	
Solid reactants: 39.00 cm^3. Solid products: 32.23 cm^3. Gel water porosity release: *small, variable & unknown.*									

Table 2. Electron densities (n_e) and mass densities (ρ) from the crystal structures, and absorption index (β) and mass attenuation coefficients (μ) from [19] for the component phases in CA cements.

Component phase	**Abbreviation**	**n_e / $e^-{\cdot}Å^{-3}$**	**ρ / g·cm^{-3}**	**β ($\times10^{-7}$)**	**μ / cm^{-1}**	**Ref.**
$CaAl_2O_4$	CA	0.88	2.96	6.27	393.9	[7]
$Ca_{12}Al_{14}O_{33}$	$C_{12}A_7$	0.80	2.68	6.83	429.3	[20]
$Ca_3Al_2(OH)_{12}$	C_3AH_6	0.78	2.53	5.56	349.6	[10]
$Ca_2Al_2O_5{\cdot}8H_2O$	C_2AH_8	0.60	1.91	3.28	206.0	[15]
$CaAl_2O_4{\cdot}10H_2O$	CAH_{10}	0.55	1.72	2.03	127.3	[8,9]
$Al(OH)_3$-gibbsite	AH_3	0.75	2.42	1.91	120.0	[21]
$Al(OH)_3$-gels[$]	*AH_3 [a]*	*0.69(2)*	*2.23(6)[#]*	*2.5(7)*	*157(44)*	*t.w.*
	AH_3 [b]	*0.61(1)*	*1.98(3)[#]*	*2.3(8)*	*145(50)*	*t.w.*
	AH_3 [c]	*0.59(2)*	*1.94(6)[#]*	*2.3(8)*	*145(50)*	*t.w.*
	AH_3 [d]	*0.56(3)*	*1.81(9)[#]*	*2.4(6)*	*151(38)*	*t.w.*

[$] The reported values are obtained from the maxima of the bivariate histograms (see Fig. 3). All β and μ values are given after correction by the 1.05 factor [22]. *[a] 50ºC sample; [b] 20ºC sample; [c] 4ºC sample; and [d] (4→50ºC) sample. [#] Mass density values derived assuming $Al(OH)_3$ stoichiometry (i.e. neglecting any gel water content).*

As the hydrates densify during conversion, see reactions (4) to (6), they ***release secondary water*** into the binder and therefore (new) ***porosity*** is formed. It is well documented that the development of porosity results in a significant loss of strength [1,2]. After conversion takes place, and a minimum strength is reached, the secondary water may continue to hydrate unhydrated CACs grains yielding a smooth long term strength gain for initial low w/c ratios [23]. However, for initial high w/c ratios, not only mechanical strength is decreased but also the additional porosity produced by conversion will favour the ingress of chemicals like chloride species. These ions may strongly affect durability, for instance inducing the corrosion of the steel bars used in reinforced concretes. Secondary water porosity development is at the heart of CACs building collapses.

To end this section, it is worth stating that although the overall chemical features of these conversion reactions are relatively well known, there are two important knowledge gaps. Firstly, the mass densities and possible water contents of the $Al(OH)_3$ gels are unknown, and secondly, the consequences of the conversion reactions in the microstructures were poorly understood. Reactions (4) and (5) produce a lot of secondary water in hardened binders but the microstructural details at the relevant length scale(s) were unknown. Furthermore, 3D X-ray imaging [24], which does not alter the sample as electron microscopies do, has not been employed to characterize these reactions.

On the other hand, 3D microstructural information can be extracted from laboratory X-ray imaging at lower resolution [24] and by synchrotron X-ray tomography with higher spatial resolution [25]. An ultimate evolution of the synchrotron imaging techniques is X-ray ptychographic tomography, a scanning technique that profits from the coherence of synchrotron X-rays [26,27]. For these imaging techniques [28], the optical elements between the sample and the detector are substituted by phase retrieval algorithms that, blended with the ptychographic methodology makes this procedure robust and reliable [29–31] yielding the amplitude and the phase of the complex-valued transmissivity of the specimen. Ptychographic tomography [26,27] at the same time yields two volumes related to the refractive index, n(r): i) the real part δ(r), and ii) the imaginary part, β(r). Hence, the full complex-valued refractive index of the specimen, $n(r)=1-\delta(r)+i\beta(r)$, can be derived [32]. It must be noted that conventional synchrotron microtomography based only on absorption contrast cannot disentangle air-based and water-based porosities [33] but ptychographic tomography at multi-keV photon energies can do it, as it yields accurate values of the electron densities [32].

Ptychographic tomography may result in isotropic three dimensional spatial resolution better than 20 nm [34] and accurate mass densities if the stoichiometries are available [35]. Mass densities for crystalline components with defined stoichiometries are a ground truth of this imaging technique as the derived values must be the same than those already reported by crystallographic means. This tomographic approach is very suitable for studying cement pastes [32,36], as the mass densities of every component phase may be determined with a high 3D resolution. From now on, the term density is employed for volumetric mass density. We employed this technique to measure the ettringite and $Al(OH)_3$ gel volume distributions in calcium sulfoaluminate pastes [37]. The densities of two aluminium hydroxide agglomerates were found out to be 2.05 and 1.50 $g{\cdot}cm^{-3}$ for two gels of approximate compositions $(CaO)_{0.12}Al(OH)_3$ and $(CaO)_{0.04}Al(OH)_3{\cdot}2.3H_2O$, respectively. Furthermore, the *in situ* hydration of a ye'elimite-gypsum paste, between 48 and 63 h, was also investigated [38]. The average ye'elimite dissolution rate was ~2 nm/min. Ptychographic tomography has been very recently used to obtain spatially resolved information, with a spatial resolution of ~100 nm, on three unaltered cement pastes: neat Portland, Portland–calcite and Portland–fly–ash blends. Data analysis yielded densities of 2.11 and 2.52 $g{\cdot}cm^{-3}$ and contents of 41.1 and 6.4 vol% for nanocrystalline C–S–H gel and poorly crystalline iron siliceous hydrogarnet, respectively. Furthermore, inner-product and outer-product C–S–H gels were characterized within the reported spatial resolution [22,39].

The conversion reactions have a very significant impact in porosity, and hence in mechanical strength and durability. The consequences of CACs conversion in mechanical strength have been

widely studied. Here, we use ptychographic nanotomography to study the $CaAl_2O_4$ hydration with the ultimate goal to understand the water porosity development in the heterogeneous conversion reactions. Chiefly, the secondary porosity has been measured with average pore sizes of ~140 nm.

2. Materials and Methods.

2.1. Material.

$CaAl_2O_4$ was synthesized by using stoichiometric amounts of $CaCO_3$ (99.95%, Alfa-Aesar) and Al_2O_3 (99.997%, Alfa-Aesar). The initial mixture was preheated at 1000°C for 6 hours and ground for 15 minutes in an agate mortar. The resulting powder was pressed (20 mm diameter and 500 MPa) and then was heated at 1450°C for 6 hours. Finally, the obtained sample was drily milled for 40 minutes (4×10 minutes) in a vibratory ball mill and then was attrition milled with isopropanol for 3 cycles of 8 minutes.

Pastes within the thin capillaries were prepared using the previously published methodology [37]. Firstly, the anhydrous powders were introduced within tapering quartz capillaries. Then, an ultrasound bath was employed to vibrate the capillaries to allow the powder to get to the tip. Secondly, the appropriated quantity of distilled water was added to attain a nominal water-to-solid (w/s) mass ratio of 1.0, and both ends of the capillary were sealed as previously reported [37]. Finally, the capillaries were manually shaken. The filled capillaries were stored at the appropriated temperatures, see just below, and synchrotron X-ray imaging data were collected after a total of 5 months of hydration. It must be clarified that the very narrow size of the capillaries, approximately 50 μm, does not allow to fully control the w/s ratio of the scanned region of the capillaries.

Different hydrating temperatures were used for each of the four studied samples. For three capillaries, the pastes were maintained for 5 months at the target temperatures: 50, 20 and 4 ºC. The fourth sample was kept at 4ºC for 2 months and then at 50ºC for the remaining 3 months to provoke conversion close to field conditions. This key sample is hereafter referred to as 4→50ºC specimen.

2.2. Analytical techniques.

2.2.1. Ptychographic nanotomography experiment. The four pastes were measured at cSAXS, Swiss Light Source, Paul Scherrer Institute (Villigen, Switzerland) by employing an instrument with positioning accuracy and stability below 10 nm [34]. Experiments were performed at a photon energy of 6.2 keV, using an identical experimental configuration to that reported in [22]. The total acquisition time for each sample including the time necessary for specimen positioning was ~15 h. Further experimental details are given in the Supplementary Information (SI).

2.2.2. Ptychographic nanotomography data processing and analysis. Ptychography reconstructions were carried out using the difference map algorithm [31] followed by a maximum likelihood refinement [40]. The resulting voxel size was 38.94 nm. The 3D spatial resolution was assessed by Fourier Shell Correlation (FSC) as previously reported [34,41].

From the d(r) tomogram, obtained from the phase projections, the 3D electron density distribution, $n_e(\boldsymbol{r})$, can be obtained according to equation (7) [35]:

$$n_e(\boldsymbol{r}) = \frac{2\pi\delta(\boldsymbol{r})}{r_0\lambda^2} \quad \textbf{(7)}$$

where r_0 is the classical electron radius and λ is the wavelength of the X-ray photons. The densities, $\rho(\boldsymbol{r})$, are determined from equation (8):

$$\rho(\boldsymbol{r}) = \frac{n_e(\boldsymbol{r})A}{N_A Z} \quad \textbf{(8)}$$

where A is the molar mass, N_A is Avogadro's number and Z is the overall amount of electrons in the formula unit. For most light elements, A/Z ≈ 2, with the notable exception of H, for which A/Z = 1.

As a consequence, for compounds containing H, an accurate conversion to densities requires the knowledge of the stoichiometry of the compound [35]. Furthermore, the linear attenuation coefficient, μ, is derived using equation (9) [32]:

$$\mu(\boldsymbol{r}) = \left(\frac{4\pi}{\lambda}\right)\beta(\boldsymbol{r}) \quad \textbf{(9)}$$

A systematic variation between the measured and theoretical attenuation coefficients was observed in all the pastes as it was previously reported [22]. The origin of this disagreement is still not clear. In a previous publication using exactly the same experimental set-up [22], we used the known attenuation coefficients for crystalline calcite and portlandite to calculate the correction parameter which was 1.05 (i.e. 5%). Here, a similar value was found for anhydrous $CaAl_2O_4$ and hence, the same correction factor, 1.05, has been applied to all attenuation coefficients. Further specific details about the tomographic reconstructions were previously reported [42].

For the electron density determination of $Al(OH)_3$ gel, the previous methodology using segmentation [22] was not possible very likely due to the small size of the particles and the associated porosity. Therefore, these values were estimated from the bivariate histograms as detailed later on.

For the segmentation of the component phases, a large volume of interest (VOI) of ~1×10^4 μm^3 for each sample was selected to carry out threshold-based image segmentation in the electron density tomogram. The reconstructed data were not filtered by denoising or smoothing. The cylindrical shape of the VOI was chosen to leave out the capillary walls and some big air pores close to the walls. This work was carried out with Avizo® Fire edition v. 8.0 (FEI Visualization Sciences Group). The materials were classified by employing the average values utilising the threshold tool. It was employed the global thresholding with histogram shape-based methods to identify the grey value which was the one closest to a valley when available. It is acknowledged that our manual histogram shape-based threshold choice may affect the accuracy of the results of the segmentations. Finally, the volume percentages of each component, or group of components, were quantitatively extracted using the material statistics tool.

Selected volumes were used to study the spatial distribution of the electron densities including water and air porosities. This analysis was performed by monitoring the evolution of the electron density value along selected directions by using ImageJ/Fiji free available software [43,44].

2.2.3. Laboratory X-ray powder diffraction. Laboratory X-ray powder diffraction data for $CaAl_2O_4$ was collected on a D8 ADVANCE (Bruker AXS) diffractometer (SCAI – Universidad de Malaga) in transmission geometry (θ/θ) which is equipped with a Johansson monochromator, using strictly monochromatic Mo-Kα_1 radiation, λ=0.7093 Å. Rietveld analysis was performed using the GSAS suite of programs and the EXPGUI graphic interface [45]. Final global optimized parameters were: background coefficients, zero-shift error, cell parameters, and peak shape parameters using a pseudo-Voigt function.

2.2.4. Sample surface area. The specific surface area for $CaAl_2O_4$ was measured by multi-point N_2 adsorption with a BET (Brunauer–Emmett–Teller) (ASAP 2420, Micromeritics, USA) instrument.

3. Results and discussion.

The Rietveld quantitative analysis of the calcium aluminate sample yielded 90.5(1) wt% of $CaAl_2O_4$ and 9.5(2) wt% of $Ca_{12}Al_{14}O_{33}$. The Rietveld plot of the starting material is given in Fig S1 and the sample had a BET surface area of 2.6 $m^2 \cdot g^{-1}$. This powder was hydrated within the capillaries as detailed in the experimental section. Very importantly, the 4→50ºC sample was hydrated at low temperature for 2 months and then at high temperature for another 3 months in order to provoke the aluminate conversion in a controlled way close to field conditions.

The volumes of the reconstructed tomograms ranged between 1.5 to 3×10^4 μm^3. These volumes are large enough to obtain a representative picture of the hydration reaction products and the resulting

microstructures. Fig. 1 displays selected orthoslices of the reconstructed electron density tomograms for each of the four studied pastes. Initially, it must be pointed out that the employed nominal w/s ratio used in the four samples, 1.0, should lead to the full hydration of the pastes. This is the case for the capillary corresponding to CA hydrated at 50 ºC (see Fig. 1a) but not for the other three samples where there are anhydrous CA microparticles. As reported previously [37,46,47], so far, it is not possible to accurately control the w/s ratio homogeneity along the full length of very small capillaries. It is known that the filling of narrow capillaries tend to decrease the w/s ratio. More research is needed to improve the experimental procedure to be able to accurately control the w/s ratios of the pastes to be analysed in narrow capillaries. The samples within very narrow capillaries are indeed needed to obtain the highest possible spatial resolution.

In addition to the reconstructed sections given in Fig. 1, Fig. S2 displays selected vertical slices of the electron density tomograms and the corresponding slices of the absorption datasets. In spite of the poorer SNR (signal to noise ratio) of the absorption tomograms in comparison with the electron density reconstructed volumes, it contained valuable additional information for component phase identification by employing the bivariate plots, see below. The 3D spatial resolutions for the $n_e(\mathbf{r})$ datasets, determined by FSC, were estimated to range between 50 and 65 nm (see Fig. S3). The spatial resolution can also be estimated from the electron density variation between the capillary wall and the air crack likely due to shrinkage. This is shown in Fig. S4 and the derived value, ~80 nm, is close to the values obtained by FSC. The 3D spatial resolutions for the $\beta(\mathbf{r})$ datasets were estimated to be close to 300 nm. The term nanotomography is employed hereafter since the determined spatial resolution of the electron density reconstructed volumes are below 100 nm.

It is also worth noting that shrinkage is evident in 4→50ºC sample, see Fig 1d. Shrinkage itself is a complex behaviour arising from different sources and the interested reader is addressed to a recent review [48]. Fig. 1a shows that the 50ºC paste is in contact with the capillary wall and that an important contribution of shrinkage after setting has not taken place. This could be partly due to the air entrainment in this sample. Conversely, Fig. 1d clearly shows shrinkage after setting as the hydrates decreased in size provoking a clear separation from the capillary wall. This is a signature of reaction 4, see Table 1. However, it is acknowledged that shrinkage has different origins and that further research is needed to firmly establish autogenous shrinkage from micro and nano tomographic studies.

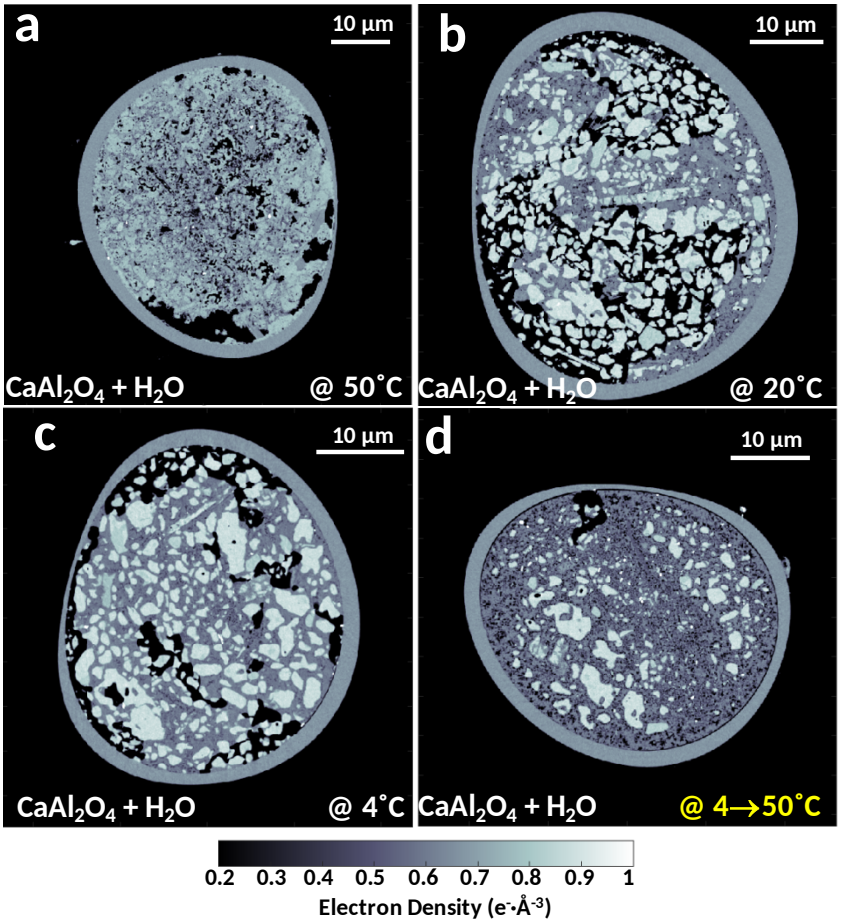

Fig. 1. Selected orthoslices of the electron density tomograms for CA pastes hydrated for 5 months. (a) at 50ºC, (b) at 20ºC, (c) at 4ºC and (d) at 4ºC for 2 months and then at 50ºC for another 3 months. Black regions within the capillaries correspond to air and water porosity, dark grey regions are due to hydrated phases and whitish grey particles are unreacted (anhydrous) materials.

$CaAl_2O_4$ hydrates as a function of temperature to give different compounds as summarized in reactions (1) to (5). Selected data, including the electron densities and attenuation coefficients, are given in Table 2. This information is key to identify the crystalline component phases, ground truth.

An overall picture of the components can be obtained from the qualitative analysis of the electron-density histograms of the VOI inside the capillaries of about $(0.6\text{-}1.4)\times10^4$ µm^3, see Fig. 2. Firstly, the shift in the air porosity peak (expected at n_e=0.00 and observed at ~0.02 e$^-$·Å^{-3}) is caused by partial volume effects as the computed region likely contain liquid/solid phases below the spatial resolution of the data. Secondly, anhydrous CA component is identified in three tomograms (20ºC, 4ºC and 4→50ºC) as it has largest electron density value, see Fig. 2, and it perfectly matches the expected crystallographic value, 0.88 e$^-$·Å^{-3}. Thirdly, it is not evident a well-defined peak in the histograms corresponding to water/pore solution that it should be located at n_e~0.33 e$^-$·Å^{-3}. In fact, the 20 and 4ºC hydrated pastes, which have the largest amount of remaining anhydrous CA, have no significant fraction of voxels within the electron density range of water porosity (including partial volume effects: $0.20 < n_e < 0.45$ e$^-$·Å^{-3}). The paste hydrated at 50ºC does not contain anhydrous CA, see Fig. 2a, and it has residual electron density in the water porosity region. Very importantly, the 4→50ºC sample, see Fig. 2d, contains anhydrous CA, likely because a low w/s ratio in the initial stage of hydration, but it also shows a significant electron density contribution in the water porosity range, very likely originated in the conversion stage when heating at 50ºC, see equations (4) to (6).

Additional details can be extracted from the study of the electron density histograms, see Fig. 2, by combining the information with that present in the bivariate histograms of the $n_e(\mathbf{r})$ and $\beta(\mathbf{r})$ datasets, see Fig. 3. For the paste hydrated at 50ºC, Fig. 2a, there are two main components severely

overlapped. However, such overlap is strongly decreased with two maxima in the bivariate plot, Fig. 3a, because the absorption of $Al(OH)_3$ gel, $\beta \sim 2.5 \cdot 10^{-7}$, is much smaller than that of $Ca_3Al_2(OH)_{12}$, $\beta = 5.56 \cdot 10^{-7}$. From the unambiguous component phase assignment, three conclusions can be drawn: (i) $Ca_2Al_2O_5 \cdot 8H_2O$ was not formed; (ii) equation (3) is firmly established; and (iii) chiefly, the electron density of the $Al(OH)_3$ gel is 0.69 $e^- \cdot Å^{-3}$, being smaller than that of gibbsite, 0.75 $e^- \cdot Å^{-3}$. Under the assumption that the gel has $Al(OH)_3$ composition, the derived mass density is 2.23 $g \cdot cm^{-3}$, significantly smaller than that of gibbsite, 2.42 $g \cdot cm^{-3}$.

For the paste hydrated at 20ºC, see Figs. 2b and 3b, there is a single peak for the $n_e(\mathbf{r})$ in the range of the hydrated phases. As expected, $Ca_3Al_2(OH)_{12}$ is not formed and equation (2) is confirmed. Since $Ca_2Al_2O_5 \cdot 8H_2O$ is crystalline and its position in the bivariate histogram is precisely situated, the n_e and β average values for $Al(OH)_3$ gel, given in Table 2, were estimated in a such way to be consistent with the broad observed maximum in the bivariate histogram. The determined density for this $Al(OH)_3$ gel is 1.98 $g \cdot cm^{-3}$. It must be highlighted the self-consistency of the results with the density of the gel obtained at 20ºC being smaller than that obtained for the sample hydrated at 50ºC. For the sake of completeness, if a stoichiometry of $Al(OH)_3 \cdot H_2O$ is assumed, one mole of gel pore water per mole of aluminium, then the derived density would be, 1.88 $g \cdot cm^{-3}$.

A similar exercise can be carried out for the paste hydrated at 4ºC but here the absence of $Ca_2Al_2O_5 \cdot 8H_2O$ cannot be ruled out because the closeness in the n_e and β average values with those of the main component, $CaAl_2O_4 \cdot 10H_2O$, Figs 2c and 3c. The electron density peak centred slightly above 0.55 $e^- \cdot Å^{-3}$ indicated that both reactions (1) and (2) took place. To estimate the electron density for $Al(OH)_3$ gel is more difficult here due to the overlapping of the three signals. The derived mass density for this $Al(OH)_3$ gel would be close to 1.9 $g \cdot cm^{-3}$.

The fourth paste, 4→50ºC, shows a very broad peak for the hydrates but that corresponding to CA is sharp, see Figs. 2d and 3d. On the one hand, it can be firmly established that $Ca_3Al_2(OH)_{12}$ was not formed and hence, reaction (5) did not take place. On the other hand, the bivariate histogram clearly shows the presence of $Ca_2Al_2O_5{\cdot}8H_2O$ and therefore, the conversion reaction (4) took place, as expected. Due to the overall shape of the bivariate data, it cannot be excluded the presence of residual $CaAl_2O_4{\cdot}10H_2O$. The mass density estimation for $Al(OH)_3$ gel for this sample, 1.89 g·cm^{-3} has a large degree of uncertainty due to the possible presence of a small amount of $CaAl_2O_4{\cdot}10H_2O$ and also because the partial volume effect.

In summary and regarding the mass densities of the $Al(OH)_3$ gels it can be stated that: (i) they are smaller than that of gibbsite, (ii) depending upon the hydrating temperature could range between 1.90 and 2.25 g·cm^{-3}, and (iii) hydration reactions at higher temperature yield $Al(OH)_3$ with higher mass densities. It is not directly deduced from our work that $Al(OH)_3$ gels densifies with time. However, the analogy of temperature and time effects, already described in literature [1], points towards reaction (6) as another source of secondary porosity.

Before tackling the study of the secondary water porosity development in the conversion reaction (4), it is important to have further insights on the spatial distribution of the component phases in the reconstructed tomograms. Fig. 4 shows selected views of the electron density for the studied pastes, where the blue electron density profiles in the right panels correspond to the yellow lines in the left panels.

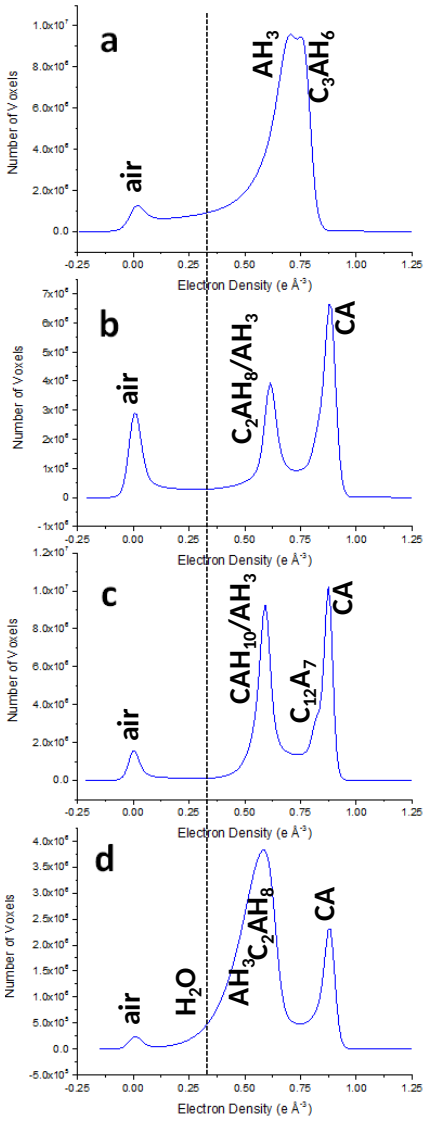

Fig. 2. Volume-of-interest histograms of the electron densities for the four studied pastes as in Fig. 1.

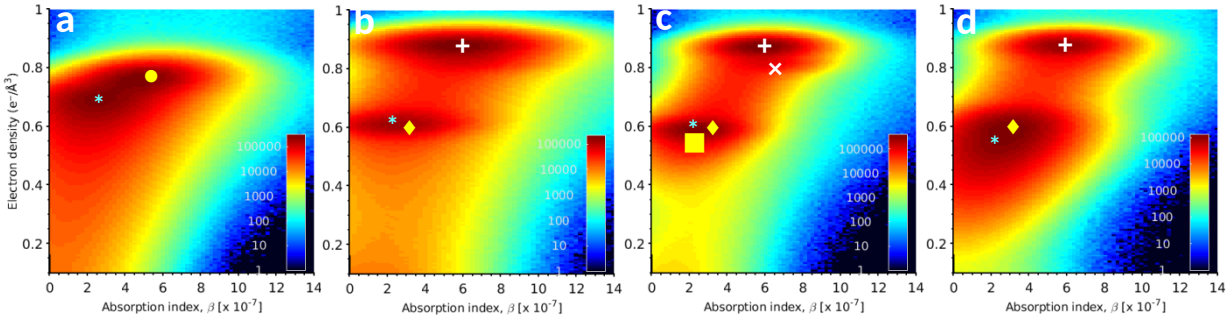

Fig. 3. Bivariate histograms of the electron densities and absorption indexes (β) for the four studied pastes arranged as in Fig. 1. The peaks arising from the different components have been labelled. The positions of the marks for nanocrystalline AH_3 gels (pale blue ∗) are derived from the maxima of the plots and these are results of this work. The marks for the crystalline phases are situated at the expected positions from their crystallographic values: Unhydrated CA (white +), unhydrated $C_{12}A_7$ (white ×), C_3AH_6 (yellow ●), C_2AH_8 (yellow ♦) and CAH_{10} (yellow ▪).

The horizontal (black) lines in the right panels (Fig. 4) correspond to the average values of the electron densities reported for the component phases in Table 2. Fig. 4a displays the electron densities for the 50ºC paste: C_3AH_6 (clearer grey) and AH_3 (darker grey), with coexisting porosity (black). Fig. 4b shows a similar plot for 20ºC paste highlighting: unreacted CA (whitish grey) and AH_3/C_2AH_8 (darker grey), with a small remaining porosity. Fig. 4c details the 4ºC paste showing unreacted CA (whitish grey) and $AH_3/C_2AH_8/CAH_{10}$ (darker grey). The crux of this work is shown in Fig. 4d, 4→50ºC paste, revealing a matrix plenty of very tiny water porosity. The electron density profile along the yellow line evolves between that of C_2AH_8, 0.60 $e^-Å^{-3}$ and that of $Al(OH)_3$, ~0.56 $e^-Å^{-3}$, with plenty of tiny porosity in between. Most of the developed porosity, due to the intentionally-provoked conversion reaction (4), have a size smaller than 200 nm and so ptychography was key as it has the required spatial resolution with contrast. It should be emphasized that widely used X-ray micro-tomography cannot reveal the porosity details in converted samples as the attained best special resolution (not voxel size) is close to 0.5 µm. There is a crack between two component phases that can be used to set a visual limit to the spatial resolution, see Fig. 4e. There is no certainty of sharp edges, but because electron densities changed from one component phase to other in four pixels, the spatial resolution has to be better than 150 nm in agreement with the FSC analysis given earlier.

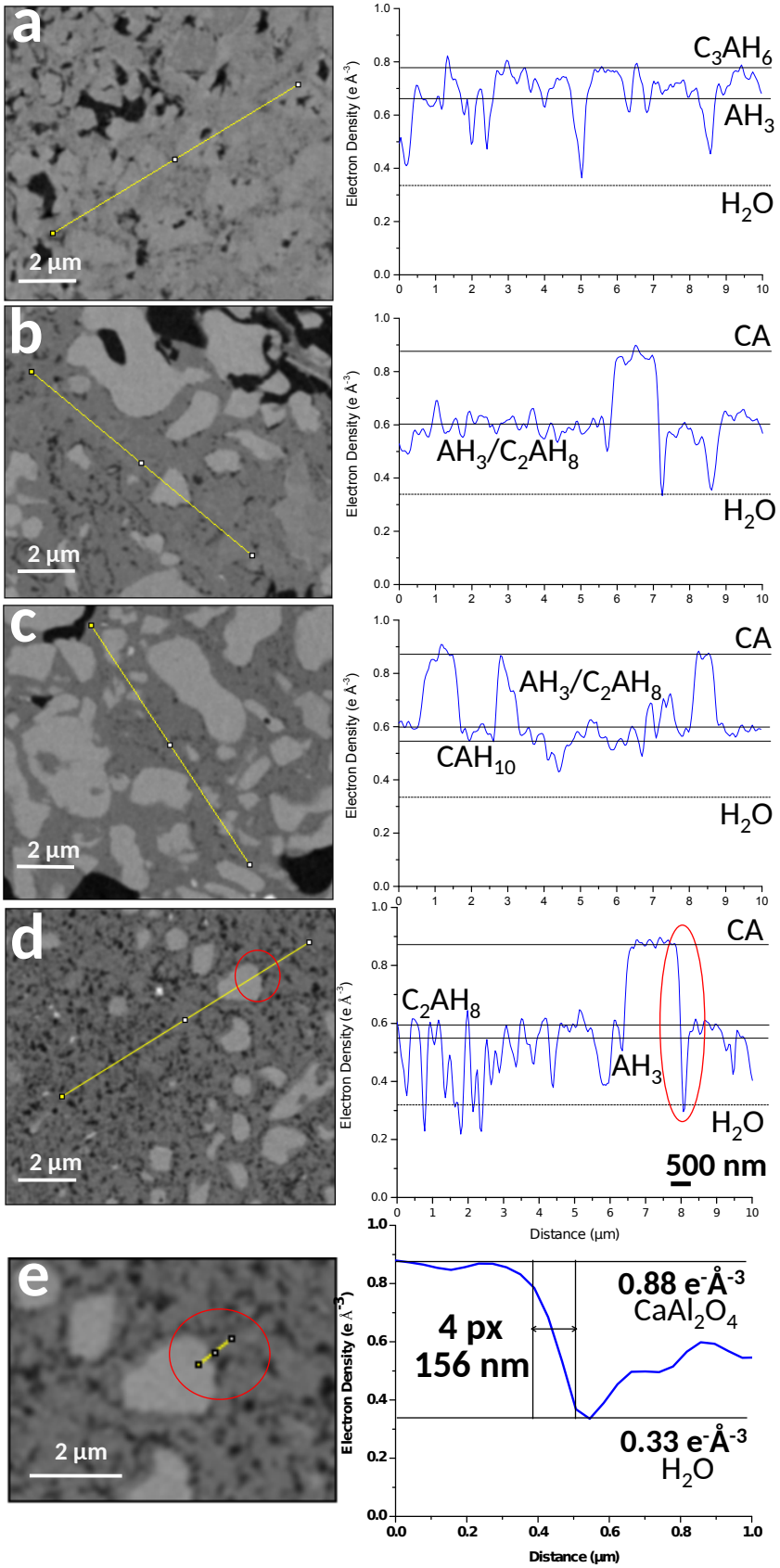

Fig. 4. (Left) selected views of the electron density tomograms and (right) electron density values corresponding to the yellow lines, with horizontal lines showing the average values of the electron densities for the component phases, those given in Table 2. (a) 50ºC, (b) 20ºC, (c) 4ºC and (d) 4→50ºC. (e) Enlarged view of a selected region in (d) to show a limit to the spatial resolution where the electron density goes from that of $CaAl_2O_4$ to that of water in four voxels.

For completeness, Figs. S5-S8 display similar plots for the four pastes at different areas of the samples to highlight that the component phase details shown in Fig. 4 are representative of the studies pastes. Fig. S9 shows a similar type of plot showing both water and air pores to show that it is possible to distinguish them from the electron density values. Furthermore, the reconstructed data have been deposited at Zenodo and hence, any interested reader/researcher could download the data and further use them.

Threshold-based segmentation of the different component phases (or set of components) has been carried out based on the electron densities. Table 3 gives the results for this data analysis. Fig. S10 displays selected views of the 3D renderings of the segmented volumes for the four pastes, showing the component spatial arrangements. For the sample hydrated at 50ºC, the derived volumes for $Al(OH)_3$ gel and C_3AH_6 were 58 and 27 vol%, respectively, which deviates from the results expected from reaction (3) based on mass balance calculations, being 40 and 45 vol%, respectively, see Table 3. We justify the overestimation of $Al(OH)_3$ gel by the partial volume effect as it likely contains residual water porosity below the spatial resolution of our measurements. Consequently, excess water, 9 vol%, is likely underestimated. The comparison of the segmentation results with the mass balance calculations reflects a poor accuracy and higher spatial resolution is needed to derive accurate volume percentages in these systems.

For the pastes hydrated at 20 and 4ºC, it was not possible to disentangle the volumes from $Al(OH)_3$ gel and the calcium aluminium hydrate phase(s) due to their very close average electron densities. However a relevant result is the presence of a large amounts of unreacted CA, ~40 vol%, which means a low w/s that it is consistent with a very low segmented content of water porosity, see Table 3. For the sample hydrated at 4ºC and then kept at 50ºC, a large amount of water porosity is segmented, 18 vol%. Itself, this large amount could come from an initial large w/s ratio but this would be incompatible with the presence of a significant amount of unreacted CA which for this sample has been segmented as 16 vol%. It cannot be ruled out that even more anhydrous CA was left by the hydration at 4ºC but a fraction of the secondary water formed by conversion (see equation 4) reacted with the stoichiometric amount of remaining CA to give more hydrated products as the segmented final water porosity, 18 vol% is smaller than the predicted value from reaction (4), 37.9 vol%. Time-resolved ptychographic nanotomography would be needed to settle this point as it could follow the conversion development and possibly the water hydration reaction with the remaining anhydrous CA component. The coexistence of a large amount of water and of anhydrous CA after five months is a firm signature of the calcium aluminate hydrate conversion. The very distinctive microstructure of the water porosity is a second signature of the conversion reaction.

Table 3. Volume percentages of the different component phases for the four studied pastes as determined by threshold-based tomographic segmentation.

Component phase	**50ºC**	**20ºC**	**4ºC**	**4→50ºC**
Air, $n_e < 0.20$ e$^-$Å^{-3} / vol%	6 // 6*	22	9	2
H_2O, 0.20 e$^-$Å^{-3} $< n_e <$ 0.45 e$^-$Å^{-3} / vol%	9 // 9*	7	3	18
AH_3, 0.45 e$^-$Å^{-3} $< n_e <$ 0.71 e$^-$Å^{-3} / vol%	58 // 40*			
C_3AH_6, $n_e > 0.71$ e$^-$Å^{-3} / vol%	27 // 45*			
AH_3/C_2AH_8, 0.45 e$^-$Å^{-3} $< n_e <$ 0.74 e$^-$Å^{-3} / vol%		30		64
AH_3/CAH_{10}, 0.45 e$^-$Å^{-3} $< n_e <$ 0.74 e$^-$Å^{-3} / vol%			48	
$CA/C_{12}A_7$, $n_e > 0.74$ e$^-$Å^{-3} / vol%		41	40	16

*Expected values based on mass balance calculations assuming: i) 100% degree of reaction, ii) w/s ratio in the scanned region of 0.51 (10% excess of water content respect to the required stoichiometric amount, 0.46), iii) the existence of 6 % of air porosity, and iv) neglecting the consequences of autogenous shrinkage.

It is also important to note that it is possible to see a clear peak corresponding to the air electron density, n_e~0 $e^-Å^{-3}$, in the histograms, see Fig. 2. Conversely, the water electron density region, n_e~0.33 $e^-Å^{-3}$, is nearly featureless. This likely has implications for the accuracy of free water segmentation which is poor. As previously discussed, higher spatial resolution is needed to obtain accurate segmentations.

Finally, we address the microstructural features of the (secondary) water porosity in the sample where the CAC conversion reaction was provoked. Data analysis was carried out with Avizo software. Because the spatial resolution of the data was estimated to be ~60 nm by FSC, the data were binned 2×2×2 and a binary output was produced where 1 was water (i.e. any voxel fulfilling $0.20 < n_e < 0.45$) and 0 for any other electron density value. Fig. 5 shows selected views of this binary output for the sample hydrated at 4ºC, see Fig. 5a, and the paste hydrated at 4ºC (identical conditions for the first 2 months) and then kept at 50ºC for another 3 months to provoke the conversion reaction, see Fig. 5b. It can be seen the relatively large amount of water porosity for the 4→50ºC sample in agreement with the plots shown in Figs. 2d and S10d. The statistical analysis of this binary dataset indicated that the water porosity has a mean pore size of 141 nm and a median pore size of 122 nm, with a variance of 195 nm. Therefore, and in agreement with the qualitative visual analysis displayed in Fig. 4d, the secondary residual porosity has an average size of 140 nm. The experimental spatial characterization of porosity at the mesoscale is key for multiscale materials modelling [49].

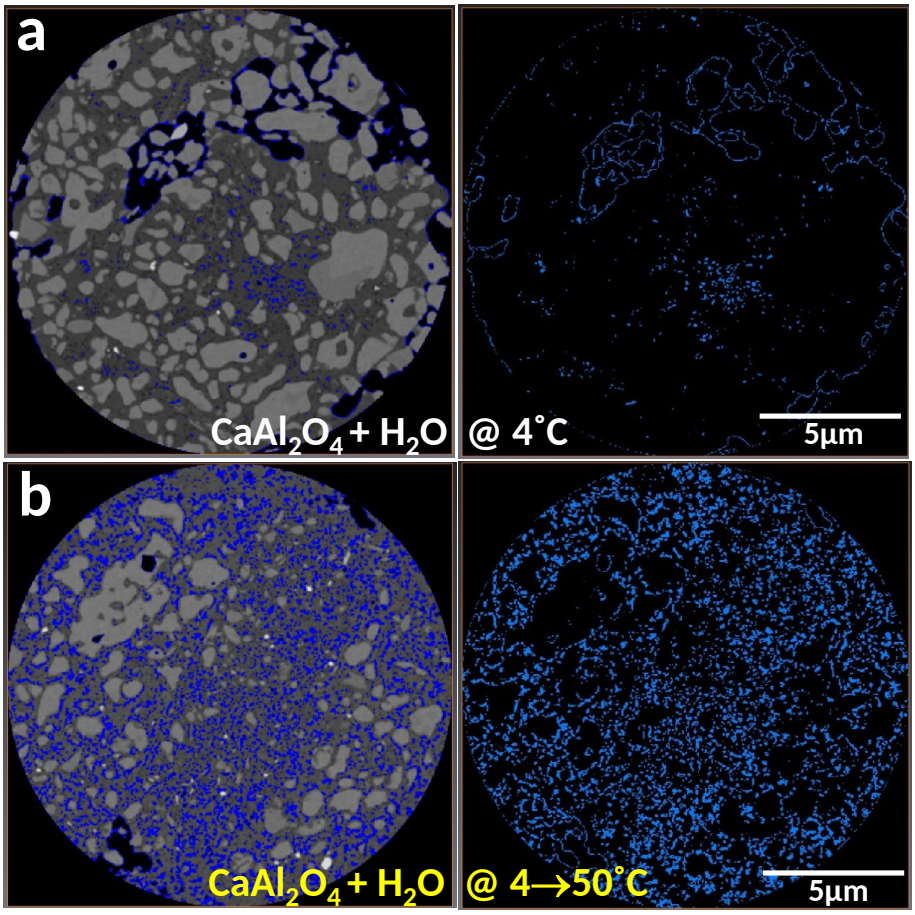

Fig. 5. Selected orthoslices of the electron density tomograms, together with water porosity (blue), for the pastes hydrated at (a) 4ºC and (b) 4ºC and then at 50ºC with the binarized water ($0.20 < n_e < 0.45$) overlaid on the full data (left) and just the plot for the water porosity (right).

This work opens the way to study the CAC conversion reaction(s) in four dimensions *by in situ* monitoring the changes in 3D water porosity with time: initially its development and later its decrease by reaction with the remaining anhydrous calcium aluminate fraction. Furthermore, the

mesostructural details of other conversion reactions in cement and other fields, like thermochemical energy storing materials [50], can also be mapped out.

4. Conclusions

X-ray synchrotron ptychographic nanotomography has been used to study the hydration products of $CaAl_2O_4$ as a function of temperature. Based on the mass density analysis of the products, the published $CaAl_2O_4$ hydration reactions have been confirmed. The novelty of this work resides firstly in the determination of the mass densities of the resulting $Al(OH)_3$ gels. Under the assumption that the gels have a $Al(OH)_3$ composition, the derived mass densities are 1.94, 1.98 and 2.23 $g{\cdot}cm^{-3}$, for samples hydrated at 4, 20 and 50ºC, respectively. These values are lower than that of $Al(OH)_3$ with gibbsite crystal structure, 2.42 $g{\cdot}cm^{-3}$, which was the reference value employed so far. Secondly, the crux of the results was the study of a sample hydrated at 4ºC for 2 months and then kept at 50ºC for 3 months to provoke CAC conversion. Ptychographic nanotomography has allowed to quantify the secondary water porosity developed with hydrate conversion. Chiefly, it has been determined that this secondary porosity develops at the mesoscale with average pore dimension of 140 nm. This result has been obtained with a specimen preparation that minimized sample-preparation related alteration(s).

Acknowledgement. Financial support from BIA2017-82391-R research grant, which is co-funded by FEDER, is gratefully acknowledged. SLS is thanked for granting beamtime at the cSAXS. Dr. Manuel Guizar-Sicairos is also thanked for his assistance with the ptychography data processing.

Data availability. The eight tomograms (four for electron densities and four for absorption) reconstructed 'raw' data in tiff format, used in this article can be freely accessed on Zenodo at https://doi.org/10.5281/zenodo.3695504, and used under the Creative Commons Attribution license.

References

[1] K.L. Scrivener, A. Capmas, Calcium aluminate cements, in: P.C. Hewlett (Ed.), Lea's Chem. Cem. Concr., 4th ed., Elsevier, 2006: pp. 713–782.

[2] K.L. Scrivener, J.L. Cabiron, R. Letourneux, High-performance concretes from calcium aluminate cements, Cem. Concr. Res. 29 (1999) 1215–1223. https://doi.org/10.1016/S0008-8846(99)00103-9.

[3] W.E. Lee, W. Vieira, S. Zhang, K. Ghanbari Ahari, H. Sarpoolaky, C. Parr, Castable refractory concretes, Int. Mater. Rev. 46 (2001) 145–167. https://doi.org/10.1179/095066001101528439.

[4] J.P. Bayoux, J.P. Letourneux, S. Marcdargent, M. Vershaeve, Acidic corrosion of high alumina cement, in: R.J. Mangabhai (Ed.), Int. Symp. Calcium Aluminate Cem., E. & F. N. Spon, London, UK, 2014: pp. 230–240.

[5] M.P. Adams, J.H. Ideker, Influence of aggregate type on conversion and strength in calcium aluminate cement concrete, Cem. Concr. Res. 100 (2017) 284–296. https://doi.org/10.1016/j.cemconres.2017.07.007.

[6] H. Pöllmann, Calcium aluminate cements - Raw materials, differences, hydration and properties, in: Rev. Mineral. Geochemistry, 2012: pp. 1–82. https://doi.org/10.2138/rmg.2012.74.1.

[7] W. Hörkner, H. Müller-Buschbaum, Zur kristallstruktur von CaAl2O4, J. Inorg. Nucl. Chem. 38 (1976) 983–984. https://doi.org/10.1016/0022-1902(76)80011-5.

[8] H.F.W. Taylor, Cement chemistry. 2nd ed., Acad. Press. 20 (1997) 335. https://doi.org/10.1016/S0958-9465(98)00023-7.

[9] N. Richard, N. Lequeux, P. Boch, Local environment of Al and Ca in CAH10 and C2AH8 by X-ray absorption spectroscopy, Eur. J. Solid State Inorg. Chem. 32 (1995) 649–662.

[10] M. Balonis, F.P. Glasser, The density of cement phases, Cem. Concr. Res. 39 (2009) 733–739. https://doi.org/10.1016/j.cemconres.2009.06.005.

[11] E.T. Allen, H.F. Rodgers, The action of caustic hydroxides on aluminium, Am. Chem. J. 24 (1900) 304–318.

[12] G. Assarsson, Reaktion zwischen Tonerdezement und Wasser, Sver. Geol. Undersbkn. 27 (1933) 26–60.

[13] T. Scheller, H.J. Kuzel, 6th International Congress on the Chemistry of Cement, in: Stud. Dicalcium Aluminate Hydrates, 1976: p. 217.

[14] J.H. Ideker, K.L. Scrivener, H. Frida, B. Touzo, Calcium Aluminate Cements, in: P.C. Hewlett, M. Liska (Eds.), Lea's Chem. Cem. Concr., 5th ed., Elsevier Ltd., 2019: pp. 537–584. https://doi.org/10.1016/B978-0-08-100773-0.00012-5.

[15] B. Raab, H. Pöllmann, "C2AH8" – 2CaO·Al2O3·(8±n)H2O – main hydration products of CAC, Z. Krist. Proc. 1 (2011) 349–354. https://doi.org/10.1524/zkpr.2011.0053.

[16] A. Cuesta, J.D. Zea-Garcia, D. Londono-Zuluaga, A.G. De La Torre, I. Santacruz, O. Vallcorba, M.A.G. Aranda, Synchrotron radiation pair distribution function analysis of gels in cements, Crystals. 7 (2017) 317. https://doi.org/10.3390/cryst7100317.

[17] D.A. Strauss Rambo, N. Ukrainczyk, F. de Andrade Silva, E. Koenders, R.D. Toledo Filho, O. da Fonseca Martins Gomes, Calcium-aluminate mortars at high temperatures: Overcoming adverse conversion effects using clinker aggregates, Cem. Concr. Compos. 96 (2019) 212–224. https://doi.org/10.1016/j.cemconcomp.2018.12.002.

[18] Y. Zhang, G. Ye, W. Gu, D. Ding, L. Chen, L. Zhu, Conversion of calcium aluminate cement hydrates at 60°C with and without water, J. Am. Ceram. Soc. 101 (2018) 2712–2717. https://doi.org/10.1111/jace.15505.

[19] B.L. Henke, E.M. Gullikson, J.C. Davis, X-Ray Interactions: Photoabsorption, Scattering, Transmission, and Reflection at E = 50− 30,000 eV, Z = 1−92, At. Data Nucl. Data Tables. 54 (1993) 181–342. https://escholarship.org/uc/item/9wh2w9rg.

[20] L. Palacios, A.G. De La Torre, S. Bruque, J.L. García-Muñoz, S. García-Granda, D. Sheptyakov, M.A.G. Aranda, Crystal structures and in-situ formation study of mayenite electrides, Inorg. Chem. 46 (2007) 4167–4176.

[21] H. Saalfeld, M. Wedde, Refinement of the crystal structure of gibbsite, A1(OH)3, Zeitschrift Fur Krist. - New Cryst. Struct. 139 (1974) 129–135. https://doi.org/10.1524/zkri.1974.139.1-2.129.

[22] A. Cuesta, A.G. De la Torre, I. Santacruz, A. Diaz, P. Trtik, M. Holler, B. Lothenbach, M.A.G. Aranda, Quantitative disentanglement of nanocrystalline phases in cement pastes by synchrotron ptychographic X-ray tomography, IUCrJ. 6 (2019) 473–491. https://doi.org/10.1107/S2052252519003774.

[23] H. Fryda, E. Charpentier, J.M. Bertino, Accelerated test for conversion of calcium aluminate cement concrete, in: C.H. Fentiman, R.J. Mangabhai, K.L. Scrivener (Eds.), Calcium Aluminate Cem. Centen. Conf., IHS BRE Press, Avignon, France, 2008.

[24] S. Brisard, M. Serdar, P.J.M. Monteiro, Multiscale X-ray tomography of cementitious materials: A review, Cem. Concr. Res. 128 (2020) 105824. https://doi.org/10.1016/J.CEMCONRES.2019.105824.

[25] M.A.G. Aranda, Recent studies of cements and concretes by synchrotron radiation crystallographic and cognate methods, Crystallogr. Rev. 22 (2016) 150–196. https://doi.org/10.1080/0889311X.2015.1070260.

[26] M. Dierolf, A. Menzel, P. Thibault, P. Schneider, C.M. Kewish, R. Wepf, O. Bunk, F. Pfeiffer, Ptychographic X-ray computed tomography at the nanoscale, Nature. 467 (2010) 436–439. https://doi.org/10.1038/nature09419.

[27] F. Pfeiffer, X-ray ptychography, Nat. Photonics. 12 (2018) 9–17. https://doi.org/10.1038/s41566-017-0072-5.

[28] J. Miao, T. Ishikawa, I.K. Robinson, M.M. Murnane, Beyond crystallography: diffractive imaging using coherent x-ray light sources., Science. 348 (2015) 530–5. https://doi.org/10.1126/science.aaa1394.

[29] J.M. Rodenburg, A.C. Hurst, A.G. Cullis, B.R. Dobson, F. Pfeiffer, O. Bunk, C. David, K. Jefimovs, I. Johnson, Hard-X-Ray Lensless Imaging of Extended Objects, Phys. Rev. Lett. 98 (2007) 034801. https://doi.org/10.1103/PhysRevLett.98.034801.

[30] M. Guizar-Sicairos, J.R. Fienup, Phase retrieval with transverse translation diversity: a nonlinear optimization approach, Opt. Express. 16 (2008) 7264. https://doi.org/10.1364/OE.16.007264.

[31] P. Thibault, M. Dierolf, O. Bunk, A. Menzel, F. Pfeiffer, Probe retrieval in ptychographic coherent diffractive imaging, Ultramicroscopy. 109 (2009) 338–343. https://doi.org/10.1016/J.ULTRAMIC.2008.12.011.

[32] J.C. da Silva, P. Trtik, A. Diaz, M. Holler, M. Guizar-Sicairos, J. Raabe, O. Bunk, A. Menzel, Mass Density and Water Content of Saturated Never-Dried Calcium Silicate Hydrates, Langmuir. 31 (2015) 3779–3783. https://doi.org/10.1021/la504478j.

[33] M.A.B. Promentilla, T. Sugiyama, T. Hitomi, N. Takeda, Characterizing the 3D pore structure of hardened Cement paste with synchrotron microtomography, J. Adv. Concr. Technol. 6 (2008) 273–286. https://doi.org/10.3151/jact.6.273.

[34] M. Holler, A. Diaz, M. Guizar-Sicairos, P. Karvinen, E. Färm, E. Härkönen, M. Ritala, A. Menzel, J. Raabe, O. Bunk, X-ray ptychographic computed tomography at 16 nm isotropic 3D resolution, Sci. Rep. 4 (2014) 3857. https://doi.org/10.1038/srep03857.

[35] A. Diaz, P. Trtik, M. Guizar-Sicairos, A. Menzel, P. Thibault, O. Bunk, Quantitative x-ray phase nanotomography, Phys. Rev. B. 85 (2012) 020104. https://doi.org/10.1103/PhysRevB.85.020104.

[36] P. Trtik, A. Diaz, M. Guizar-Sicairos, A. Menzel, O. Bunk, Density mapping of hardened cement paste using ptychographic X-ray computed tomography, Cem. Concr. Compos. 36 (2013) 71–77. https://doi.org/10.1016/J.CEMCONCOMP.2012.06.001.

[37] A. Cuesta, A.G. De la Torre, I. Santacruz, P. Trtik, J.C. da Silva, A. Diaz, M. Holler, M.A.G. Aranda, Chemistry and Mass Density of Aluminum Hydroxide Gel in Eco-Cements by Ptychographic X-ray Computed Tomography, J. Phys. Chem. C. 121 (2017) 3044–3054. https://doi.org/10.1021/acs.jpcc.6b10048.

[38] A. Cuesta, A.G. De la Torre, I. Santacruz, P. Trtik, J.C. Da Silva, A. Diaz, M. Holler, M.A.G. Aranda, In situ hydration imaging study of a ye'elimite paste by ptychographic X-ray computed tomography, in: 39th Int. Conf. Cem. Microsc. ICMA 2017, 2017: pp. 17–32.

[39] M.A.G. Aranda, A. Cuesta, A.G. De la Torre, P. Trtik, A. Diaz, Ptychographic X-ray computed tomography analysis of cement pastes, in: 15th Int. Congr. Chem. Cem., 2019: pp. 1–12.

[40] P. Thibault, M. Guizar-Sicairos, Maximum-likelihood refinement for coherent diffractive imaging, New J. Phys. 14 (2012) 063004. https://doi.org/10.1088/1367-2630/14/6/063004.

[41] M. van Heel, M. Schatz, Fourier shell correlation threshold criteria, J. Struct. Biol. 151 (2005) 250–262. https://doi.org/10.1016/j.jsb.2005.05.009.

[42] M. Guizar-Sicairos, A. Diaz, M. Holler, M.S. Lucas, A. Menzel, R.A. Wepf, O. Bunk, Phase tomography from x-ray coherent diffractive imaging projections, Opt. Express. 19 (2011) 21345. https://doi.org/10.1364/OE.19.021345.

[43] M.D. Abràmoff, P.J.J. Magalhães, S.J. Ram, Image Processing with ImageJ, Biophotonics Int. 11 (2004) 36–42. https://imagescience.org/meijering/publications/1115/ (accessed September 25, 2018).

[44] J. Schindelin, I. Arganda-Carreras, E. Frise, V. Kaynig, M. Longair, T. Pietzsch, S. Preibisch, C. Rueden, S. Saalfeld, B. Schmid, J.-Y. Tinevez, D.J. White, V. Hartenstein, K. Eliceiri, P. Tomancak, A. Cardona, Fiji: an open-source platform for biological-image analysis, Nat. Methods. 9 (2012) 676–682. https://doi.org/10.1038/nmeth.2019.

[45] A.C. Larson, R.B. Von Dreele, General structure analysis system (GSAS), Los Alamos Natl. Lab. Rep. LAUR. 748 (2004) 86–748.

[46] E. Gallucci, K. Scrivener, A. Groso, M. Stampanoni, G. Margaritondo, 3D experimental investigation of the microstructure of cement pastes using synchrotron X-ray

microtomography (μCT), Cem. Concr. Res. 37 (2007) 360–368. https://doi.org/10.1016/j.cemconres.2006.10.012.

[47] M. Parisatto, M.C. Dalconi, L. Valentini, G. Artioli, A. Rack, R. Tucoulou, G. Cruciani, G. Ferrari, Examining microstructural evolution of Portland cements by in-situ synchrotron micro-tomography, J. Mater. Sci. 50 (2015) 1805–1817. https://doi.org/10.1007/s10853-014-8743-9.

[48] L. Wu, N. Farzadnia, C. Shi, Z. Zhang, H. Wang, Autogenous shrinkage of high performance concrete: A review, Constr. Build. Mater. 149 (2017) 62–75. https://doi.org/10.1016/j.conbuildmat.2017.05.064.

[49] S. Yip, M.P. Short, Multiscale materials modelling at the mesoscale, Nat. Mater. 12 (2013) 774–777. https://doi.org/10.1038/nmat3746.

[50] B. Chen, F. Kuznik, M. Horgnies, K. Johannes, V. Morin, E. Gengembre, Physicochemical properties of ettringite/meta-ettringite for thermal energy storage: Review, Sol. Energy Mater. Sol. Cells. 193 (2019) 320–334. https://doi.org/10.1016/j.solmat.2018.12.013.

Supplementary Information for

Calcium aluminate cement conversion analysed by ptychographic nanotomography

S. Shirani[1,#] A. Cuesta[1,#] A. G. De la Torre[1], A. Diaz[2], P. Trtik[2], M. Holler[2], M. A. G. Aranda[1]*

[1]*Departamento de Química Inorgánica, Cristalografía y Mineralogía, Universidad de Málaga, Málaga, 29071, Spain.*

[2]*Paul Scherrer Institut, 5232 Villigen PSI, Switzerland*

[#] *These authors have contributed equally*

* *email: g_aranda@uma.es*

This PDF file includes:

Data availability description.

Extended Materials and Methods including Table S1.

Figure S1. Rietveld Quantitative Phase Analysis (RQPA) for the CA sample

Figure S2. (left) Selected orthoslices of the electron density tomograms and (right) of the absorption tomograms for CA pastes hydrated for 5 months (a) at 50ºC, (b) at 20ºC, (c) at 4ºC and (d) at 4ºC for 2 months and at 50ºC for another 3 months. Black regions within the capillaries correspond to porosity (air and water), dark grey regions are due to hydrated component phases and whitish grey particles are unreacted (anhydrous) materials.

Figure S3. Fourier Shell Correlation plots from electron density tomograms for CA pastes hydrated for 5 months (a) at 50ºC, (b) at 20ºC, (c) at 4ºC and (d) at 4ºC for 2 months and at 50ºC for another 3 months.

Figure S4. (Left) selected view of the electron density tomogram for the CA paste hydrated at 4ºC for 2 months and at 50ºC for another 3 months. The inset shows an enlarged view with an air crack very likely due to shrinkage. (Right) electron density values corresponding to the yellow line in the inset of the left panel where it can be seen that electron density sharply drops from the value of the capillary (0.68 $e^{-}Å^{-3}$) to that of the air (ideally 0.00 $e^{-}Å^{-3}$ but it is observed at 0.05 $e^{-}Å^{-3}$ likely due to the partial volume effect). The profile shows that the electron density evolves in 4-5 pixels (voxels) and that the change between 75% and 25% of the electron densities take place in two pixels (78 nm). This crack has a size of about 9 pixels or 350 nm.

Figure S5. (Left) Two selected views of the electron density tomograms, and (right) electron density values corresponding to the yellow lines in the left panels for the CA paste hydrated at 50ºC for 5 months.

Figure S6. (Left) Two selected views of the electron density tomograms, and (right) electron density values corresponding to the yellow lines in the left panels for the CA paste hydrated at 20ºC for 5 months.

Figure S7. (Left) Two selected views of the electron density tomograms, and (right) electron density values corresponding to the yellow lines in the left panels for the CA paste hydrated at 4ºC for 5 months.

Figure S8. (Left) Two selected views of the electron density tomograms, and (right) electron density values corresponding to the yellow lines in the left panels for the CA paste hydrated at 4ºC for 2 months and at 50ºC for another 3 months.

Figure S9. (Left) selected view of the electron density tomogram for the CA paste hydrated at 4ºC for 2 months and at 50ºC for another 3 months. The two insets show enlarged views (top) water and air porosities and (bottom) further enlarged view for an air pore. (Right) electron density values corresponding to the yellow lines in the insets of the left panels where it can be seen the evolution of the electron densities. $CaAl_2O_4$ (0.88 $e^-Å^{-3}$), C_2AH_8 (0.60 $e^-Å^{-3}$), AH_3 (~0.56 $e^-Å^{-3}$), H_2O (0.33 $e^-Å^{-3}$) and air (0.00 $e^-Å^{-3}$). In some cases the water and air porosities does not reach the theoretical values due to the partial volume effect in tiny pores.

Figure S10. 3D renderings of the segmented volumes showing the components for CA pastes hydrated for 5 months (a) at 50ºC, (b) at 20ºC, (c) at 4ºC and (d) at 4ºC for 2 months and at 50ºC for another 3 months.

Data availability. All tomographic raw data files, in tiff format, used in this work have been deposited on Zenodo, https://doi.org/10.5281/zenodo.3695504, to be used under the Creative Commons Attribution license. The information about the code used for the upload files is the follow:

CA-50 ºC sample: 50C-CA.rar folder

tomo_beta_ S06105to_S07418_Hann_freqscl_0.35_0xxx
tomo_delta_S06105_to_S07418_Hann_freqscl_1.00_0xxx

CA-20 ºC sample: 20C-CA.rar folder

tomo_beta_S07430_to_S08750_Hann_freqscl_0.35_0xxx
tomo_delta_S07430_to_S08750_Hann_freqscl_1.00_0xxx

CA-4 ºC sample: 4C-CA.rar folder

tomo_beta_ S00040_to_S00864_Hann_freqscl_0.35_0xxx
tomo_delta_S00040_to_S00864_Hann_freqscl_1.00_0xxx

CA-4 ºC and 50 ºC sample: 4+50C-CA.rar folder

tomo_beta_ S08765_to_S10071_Hann_freqscl_0.35_0xxx
tomo_delta_S08765_to_S10071_Hann_freqscl_1.00_0xxx

Extended Materials and Methods

PXCT experiments and data processing.

PXCT experiments and data processing.

The PXCT experiments took place at the cSAXS beamline at the Swiss Light Source, Paul Scherrer Institute in Villigen, Switzerland, using the same experimental parameters as those reported in Ref. [1] in the main article. In table S1 we report the ptychographic and tomographic acquisition parameters corresponding to each sample, namely: the field of view (FOV) (horizontal × vertical),

step size and acquisition time at each point in the ptychographic scans, and the number of tomographic angular projections (Np). For the dose estimation we used the same procedure as the one described in Ref. [1]. We found that the dose imparted on all samples was about 3×10^7 Gy, estimated for CA, which is one of the material phases with highest absorption in these samples. This means that, for the other materials, the deposited dose is less.

Sample	FOV* (μm^2)	step (μm)	t (s)	N_p
50°C	73×26	3	0.08	1300
20°C	58×15	3	0.08	1300
4°C	50×25	2.6	0.1	800
4°C → 50°C	60×12	3	0.08	1300

Table S1: acquisition parameters used for the recording of the data by ptychographic tomography: field of view of ptychographic scans for each tomographic projection (FOV horizontal × vertical), average step size in the scans (step), exposure time at each scanning position (t) and number of tomographic projections (N_p).

Ptychographic reconstructions and tomographic reconstruction were performed in an identical way as reported in the supplementary information of Ref. [1].

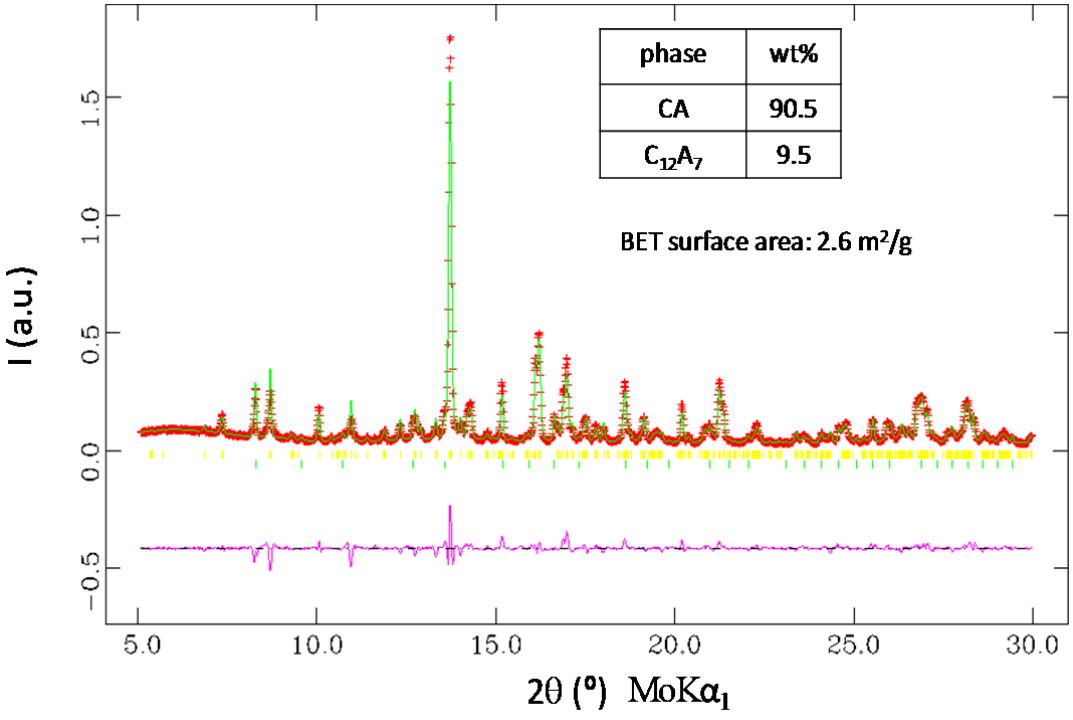

Figure S1. Rietveld Quantitative Phase Analysis (RQPA) for the CA sample.

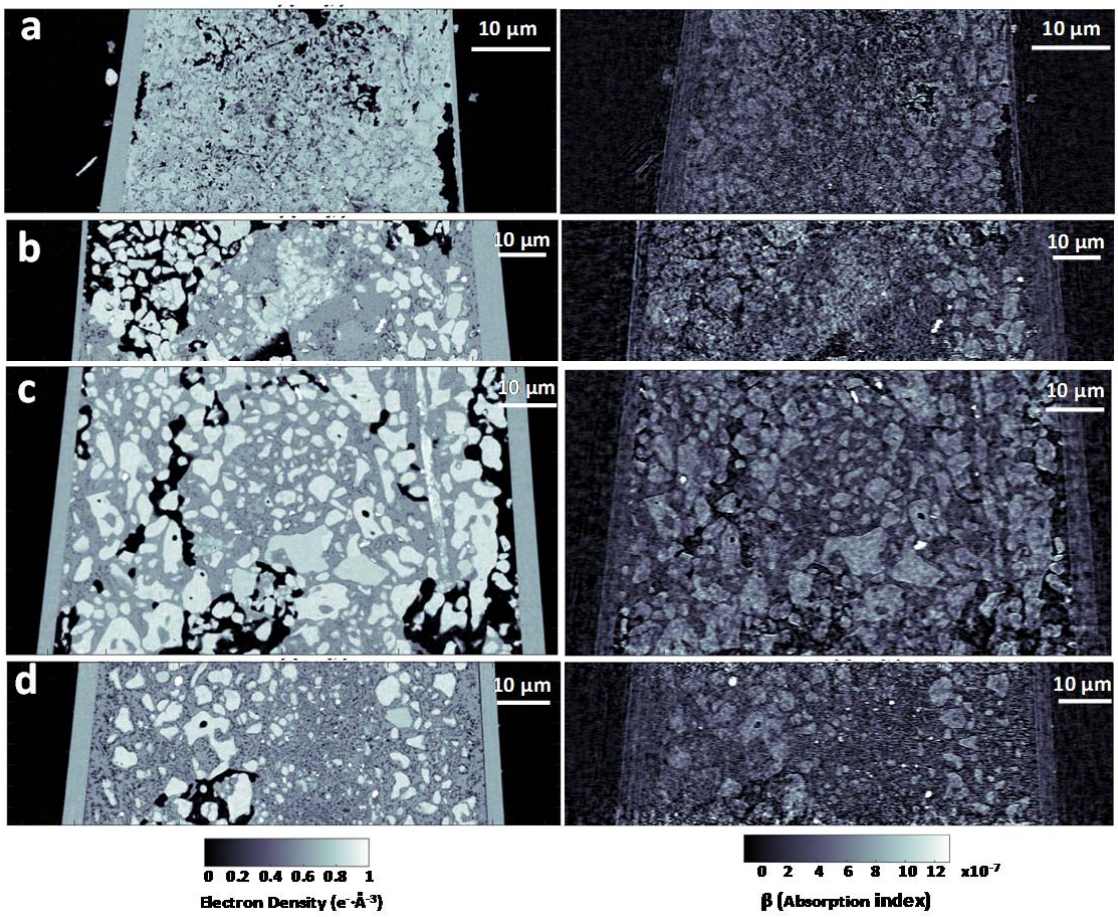

Figure S2. (left) Selected vertical slices of the electron density tomograms and (right) of the absorption tomograms for CA pastes hydrated for 5 months (a) at 50ºC, (b) at 20ºC, (c) at 4ºC and (d) at 4ºC for 2 months and at 50ºC for another 3 months. Black regions within the capillaries correspond to porosity (air and water), dark grey regions are due to hydrated component phases and whitish grey particles are unreacted (anhydrous) materials.

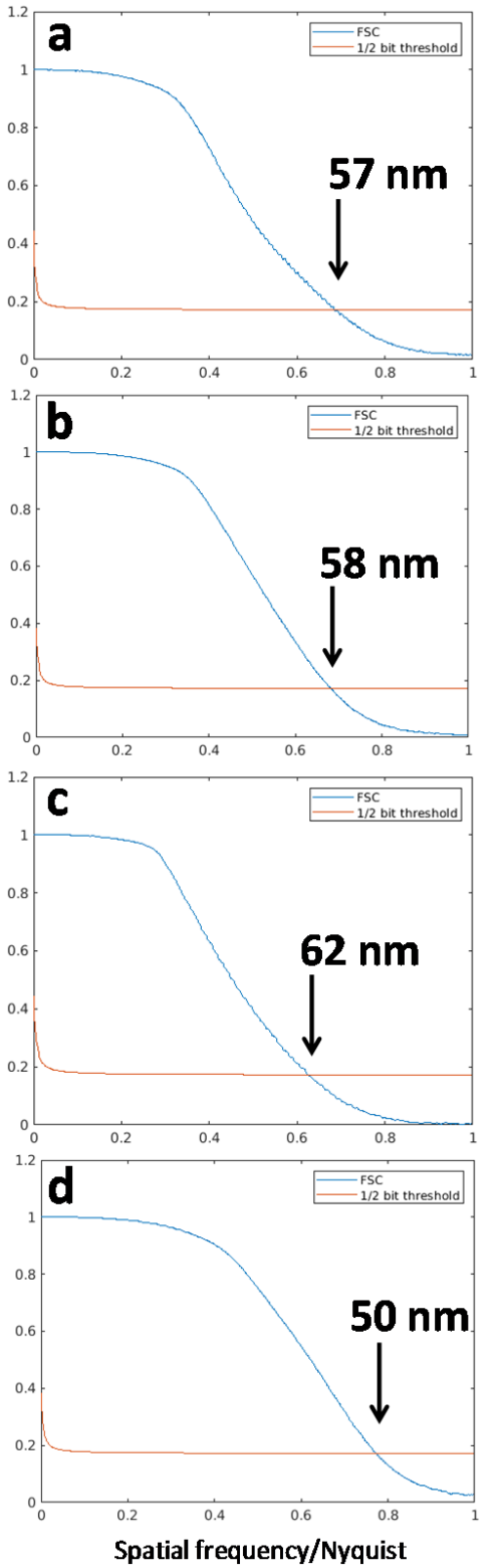

Figure S3. Fourier Shell Correlation plots from electron density tomograms for CA pastes hydrated for 5 months (a) at 50ºC, (b) at 20ºC, (c) at 4ºC and (d) at 4ºC for 2 months and at 50ºC for another 3 months.

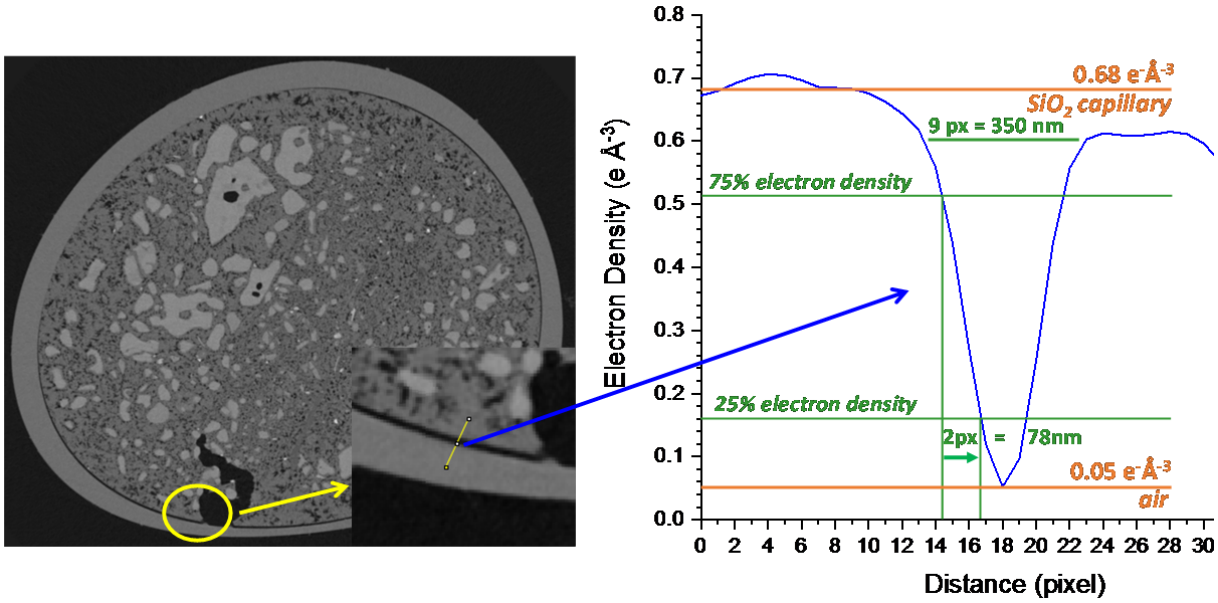

Figure S4. (Left) selected view of the electron density tomogram for the CA paste hydrated at 4ºC for 2 months and at 50ºC for another 3 months. The inset shows an enlarged view with an air crack very likely due to shrinkage. (Right) electron density values corresponding to the yellow line in the inset of the left panel where it can be seen that electron density sharply drops from the value of the capillary (0.68 $e^{-}Å^{-3}$) to that of the air (ideally 0.00 $e^{-}Å^{-3}$ but it is observed at 0.05 $e^{-}Å^{-3}$ likely due to the partial volume effect). The profile shows that the electron density evolves in 4-5 pixels (voxels) and that the change between 75% and 25% of the electron densities take place in two pixels (78 nm). This crack has a size of about 9 pixels or 350 nm.

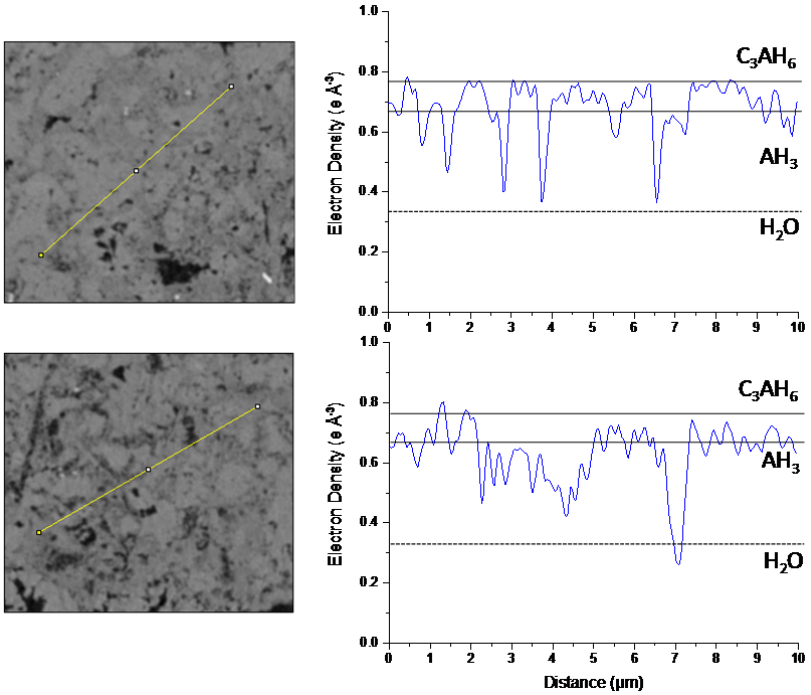

Figure S5. (Left) Two selected views of the electron density tomogram, and (right) electron density values corresponding to the yellow lines in the left panels for the CA paste hydrated at 50ºC for 5 months.

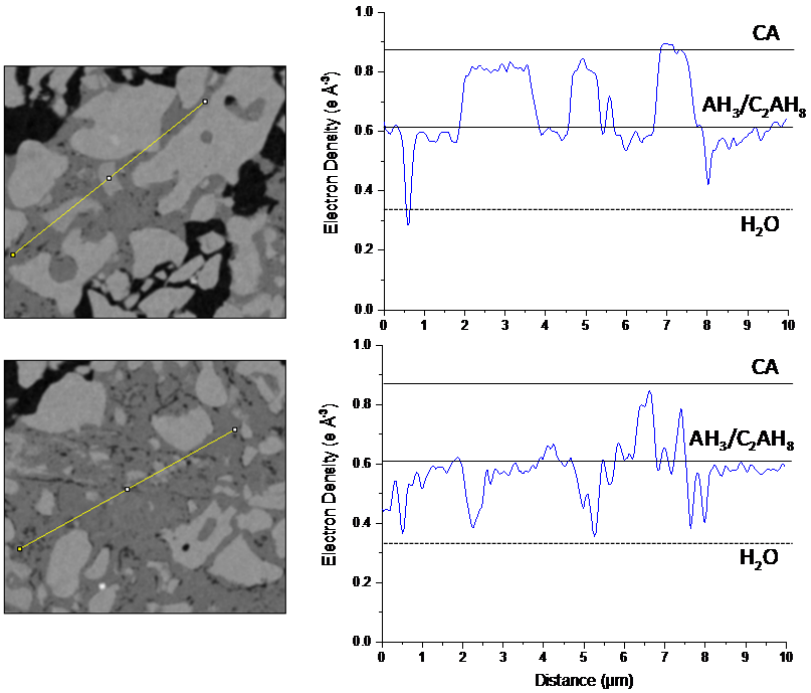

Figure S6. (Left) Two selected views of the electron density tomogram, and (right) electron density values corresponding to the yellow lines in the left panels for the CA paste hydrated at 20ºC for 5 months.

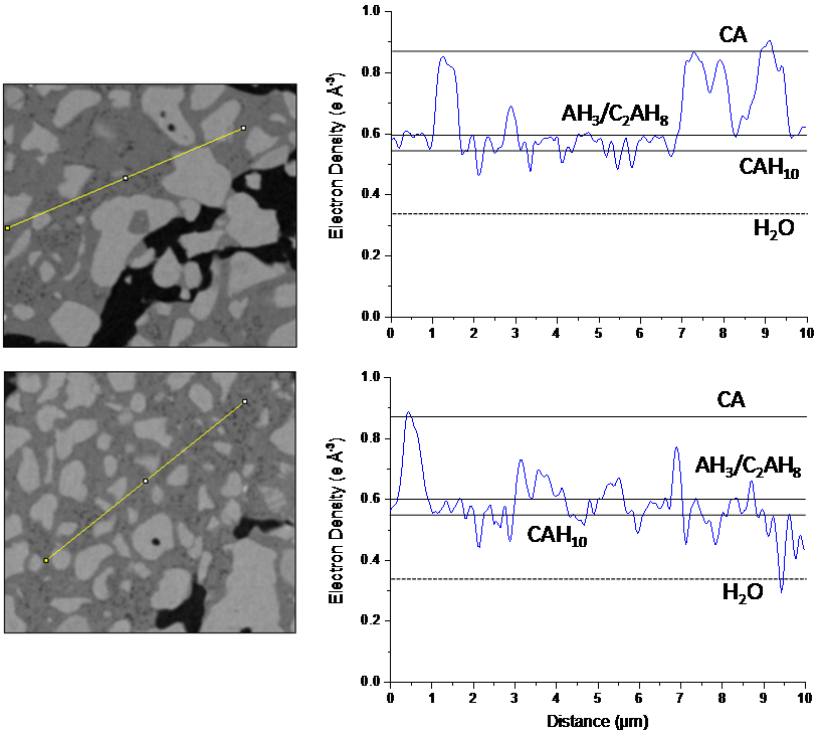

Figure S7. (Left) Two selected views of the electron density tomogram, and (right) electron density values corresponding to the yellow lines in the left panels for the CA paste hydrated at 4ºC for 5 months.

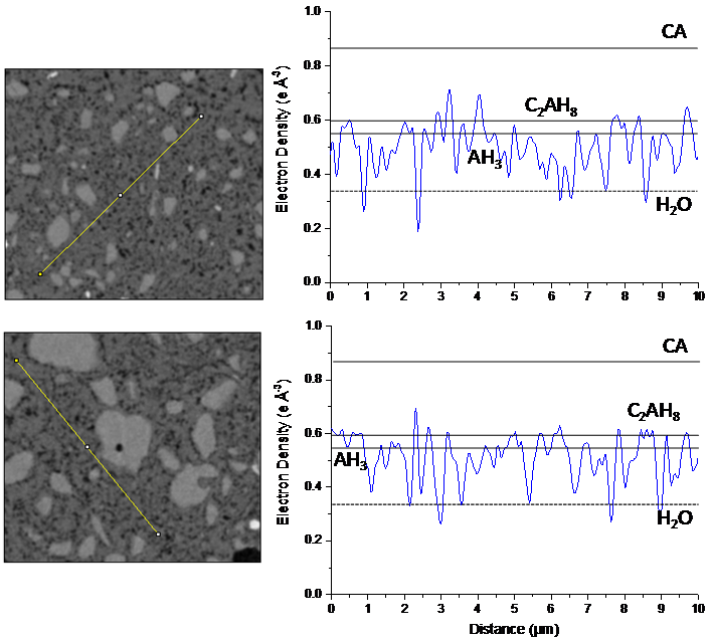

Figure S8. (Left) Two selected views of the electron density tomogram, and (right) electron density values corresponding to the yellow lines in the left panels for the CA paste hydrated at 4ºC for 2 months and at 50ºC for another 3 months.

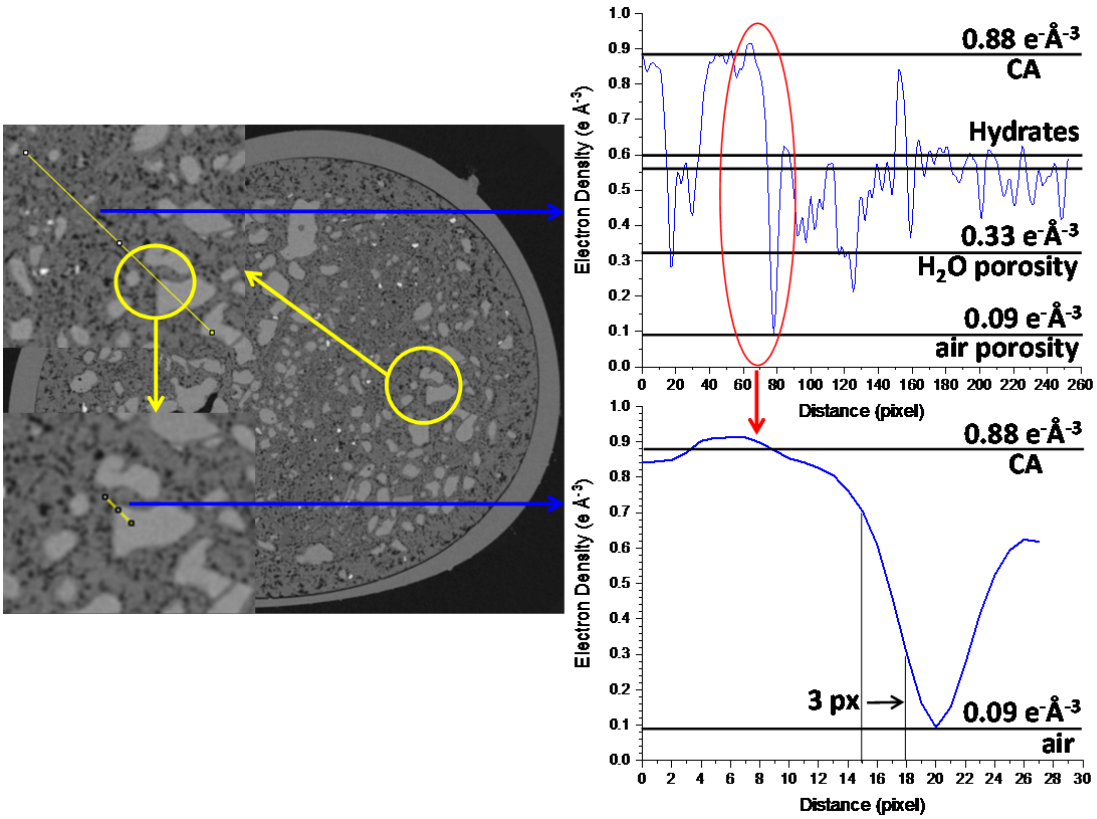

Figure S9. (Left) selected view of the electron density tomogram for the CA paste hydrated at 4ºC for 2 months and at 50ºC for another 3 months. The two insets show enlarged views (top) water and air porosities and (bottom) further enlarged view for an air pore. (Right) electron density values corresponding to the yellow lines in the insets of the left panels where it can be seen the evolution of the electron densities. $CaAl_2O_4$ (0.88 e$^-$Å^{-3}), C_2AH_8 (0.60 e$^-$Å^{-3}), AH_3 (~0.56 e$^-$Å^{-3}), H_2O (0.33 e$^-$Å^{-3}) and air (0.00 e$^-$Å^{-3}). In some cases the water and air porosities does not reach the theoretical values due to the partial volume effect in tiny pores.

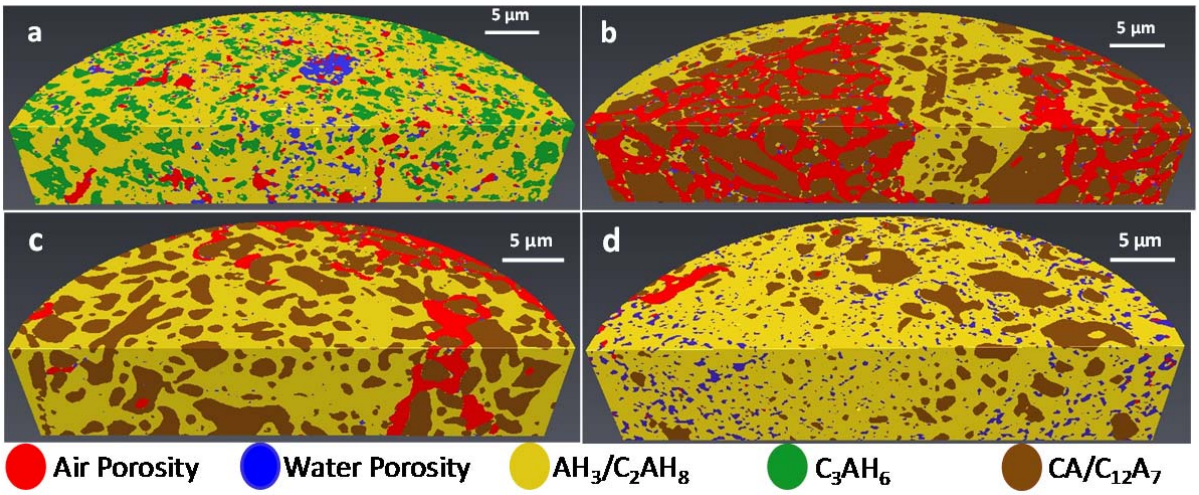

Figure S10. 3D renderings of the segmented volumes showing the components for CA pastes hydrated for 5 months (a) at 50ºC, (b) at 20ºC, (c) at 4ºC and (d) at 4ºC for 2 months and at 50ºC for another 3 months.

References

1. Cuesta, A. *et al.* Quantitative disentanglement of nanocrystalline phases in cement pastes by synchrotron ptychographic X-ray tomography. *IUCrJ* **6**, 473–491 (2019).